Application of cubic spline interpolation with optimal spatial sampling for damage identification

Leonardo Pedroso[1], António Arco[1], Iara Figueras[1], José Viriato Araújo dos Santos[1], and Hernâni Lopes[2]

[1]*IDMEC, Instituto Superior Técnico, Universidade de Lisboa, Lisboa, Portugal*
[2]*DEM, ISEP, Instituto Politécnico do Porto, Porto, Portugal*

Accepted version[1]

Accepted on 18 Aug 2021

Cite as

L. Pedroso, A. Arco, I. Figueiras, J. V. Araújo dos Santos, J. L. M. Fernandes, and H. Lopes, 'Application of cubic spline interpolation with optimal spatial sampling for damage identification', *Structural Control and Health Monitoring*, vol. 29, no. 1, p. e2856, 2022. doi: 10.1002/stc.28560.

Received: Added at production | Revised: Added at production | Accepted: Added at production

DOI: xxx/xxxx

ARTICLE TYPE

Application of cubic spline interpolation with optimal spatial sampling for damage identification

L. Pedroso[1] | A. Arco[1] | I. Figueiras[1] | J.V. Araújo dos Santos*[1] | J.L.M. Fernandes[1] | H. Lopes[2]

[1]IDMEC, Instituto Superior Técnico, Universidade de Lisboa, Lisboa, Portugal
[2]DEM, ISEP, Instituto Politécnico do Porto, Porto, Portugal

Correspondence
*J.V. Araújo dos Santos. Email: viriato@tecnico.ulisboa.pt

Present Address
Av. Rovisco Pais, 1049-001 Lisboa, Portugal

Summary

This paper aims to explore a new technique for structural damage identification using cubic spline interpolation. The method is based on the interpolation of modal rotations measured with shearography, making use of the analytical derivative of the spline to compute the modal curvature, which is known to be very sensitive to damage. As a means of reducing noise and measurement uncertainty propagation to a minimum, an expression for an optimal spatial sampling is derived. Furthermore, a baseline-free damage factor, allied with an optimal sampling, is also introduced. The proposed identification method is validated using experimental data of a beam. Using a damage localisation quality index, a comparison between the present method and one using finite differences is carried out, showing that the differentiation of spline interpolation leads to better damage identifications. The results obtained with the proposed approach show robustness and consistency in the localisations. Additionally, the hurdles of identifying small and multiple damage are tackled with the proposed method, yielding a good performance.

KEYWORDS:
Damage identification,Optimal sampling, Multiple damage, Shearography, Cubic spline interpolation, Beam

Nomenclature

μ	damage localisation quality index
θ	modal rotation field of the undamaged structure
$\tilde{\theta}$	modal rotation field of the damaged structure
$\breve{\theta}$	measured modal rotation field of the damaged structure
$E^{(u)}$	error associated with noise and measurement uncertainty
$E^{(p)}$	error associated with the propagation of noise and measurement uncertainty after diferentiation
$E^{(m)}$	error associated with the use of spline interpolation as an approximation of the derivative

$E^{(t)}$ error associated with the combination of all error sources (total error)

$h^{(\text{opt})}$ optimal spatial sampling interval

h uniform spatial sampling interval

q modal rotation number

N number of measured modal rotations

s cubic spline

m_i second derivative of the spline function evaluated in node x_i

δb absolute error in vector **b**

δm error propagated to vector **m**

β average sum of the error weights

ACDF adjusted curvature damage factor

$F^{(m)}(x)$ robust fit of $\partial\tilde{\theta}_q(x)/\partial x$

$\hat{DF}$ normalised damage factor

MCDF modified curvature damage factor

1 | INTRODUCTION

Structural damage identification is a field with great social and economical impact, since it provides a solution to the prevention of structural failure, whose occurrence leads to catastrophic harm, especially as far as public-safety is concerned. Given this fact, it is essential to have a range of methods that are able to efficiently monitor structural integrity and identify potential damaged areas. Such techniques prove to be quite useful across various engineering fields, namely mechanical, civil, aeronautical, aerospace and naval engineering. In view of its implications, researchers have been giving much attention to this field over the past decades and a wide spectrum of methods arose, whose ultimate goal is to detect, localise and quantify the damage present in a structure. Indeed, Rytter[1] suggested the categorisation of a damage identification scheme by four identification levels, which is followed in this paper. These increasingly complex levels comprise, respectively: (i) Detection, which indicates the presence of damage; (ii) Localisation, which gives information about where is the damage located in the structure; (iii) Assessment, which provides insight into the size of the damage; (iv) Consequence, which evaluates the safety conditions and the remaining life of the structure. Almost exclusive consideration has been given to non-destructive inspection methods because of their broader applicability. Among them one can highlight acoustic, ultrasonic, radiographic, magnetic, vibrational, thermographic and eddy current based techniques. In particular, vibration based schemes for damage identification, which have been subjected to plenty of research throughout the past couple of decades, became very popular, although many of the proposed methods do not fully meet the expectations.

The underlying principle of a vibration based scheme is the fact that a localised damage changes the local dynamic characteristics of a structure, thus measuring its dynamic response provides useful information to the identification of the damage. Furthermore, such schemes allow for global identification methods not requiring the *a priori* knowledge of the vicinity or the site of the damage, as many others do. Moreover, as it was put forward by Pandey *et al.*[2], by using numerical examples, the analysis of the curvature mode shape, *i.e.* the second spatial derivative of the vibrational displacement mode shape, and comparison with its undamaged counterpart, reveals a localised anomaly where the damage is located.

The state-of-the-art approaches are detailed in Table 1. However, only a small amount of research has been done on directly exploring the properties of cubic spline interpolation as a means of obtaining an approximation of the modal curvature fields[3,4,5]. The major drawback of using finite differences to estimate derivatives is the fact that measurement uncertainty and noise are propagated and amplified, and, therefore, one needs to mitigate such effects. Sazonov and Klinkhachorn[6] computed the modal

curvature shape by applying finite differences to approximate the second derivative of the modal displacement. They also provided an optimal spatial sampling interval in order to minimise the effects of noise and measurement error and their propagation, which was validated by numerical examples. Moreno-García *et al.*[7] also developed an optimal spatial sampling interval to minimise the noise and measurement error amplification, in the approximation of the first four derivatives of the modal displacement on a composite plate. Mininni *et al.*[8] presented a method based on the computation of the curvature mode shape via finite differences of modal rotation fields of a beam, *i.e.* the first spatial derivative of the vibrational displacement mode shape, obtained experimentally using shearography. As thoroughly described in Francis *et al.*[9] and Araújo dos Santos *et al.*[10], shearography is an optical technique which enables the measurement of the gradient of the displacement fields. Not only is this technique not as prone to noise as the one proposed by Sazonov and Klinkhachorn[6], since it requires only the approximation of a first derivative, but also an optimal spatial sampling was derived.

TABLE 1 State of the art approaches.

Reference	Type of structure	Data	Post-processing technique
[2]	Cantilever and simply supported analytical beam	Numeric	Finite differences
[11]	Simply supported and continuous beams	Numeric/Experimental	Finite differences
[6]	Aluminum beam	Numeric	Finite differences
[12]	Cantilever beam	Experimental	Finite differences
[13]	Aluminium beams	Experimental	Finite differences
[14]	Simple supported beam	Numeric	Finite differences
[15]	Cantilever beams	Numeric/Experimental	Finite differences
[7]	Laminated composite plate	Numeric	Finite differences
[16]	Laminated composite plates	Numeric	Finite differences
[8]	Beam	Experimental	Finite differences
[17]	Beam	Experimental	Finite differences
[18]	Cantilever beam	Numeric/Experimental	Finite differences
[19]	Bridge structures	Numeric	Finite differences
[20]	Euler–Bernoulli beams	Numeric	Finite differences
[21]	Interstate 40 bridge	Experimental	Finite differences
[22]	Plexiglas cantilever beam and steel plate	Experimetal	Wavelet transform
[23]	Cantilever plate/FRP composite plate	Numeric/Experimental	Wavelet transform
[24]	Cantilever beam	Numeric/ Experimental	Wavelet transform
[25]	Fully clamped square layered composite plate	Numeric	Wavelet transform
[26]	Euler–Bernoulli beam component (EBC)	Numerical/Experimental	Wavelet transform
[27]	Cantilever steel beam with a stationary roving mass	Experimental	Wavelet transform
[28]	Cantilever and a simple supported beam	Numeric	Wavelet transform
[29]	Damaged plate	Numeric/Experimental	Wavelet transform
[30]	Damaged beams	Numeric	Wavelet transform

Nevertheless, the results obtained by these researchers are not fully satisfactory. In fact, even considering an optimal sampling, there are oscillations induced by the noise propagation such that it is difficult to localise small damage and experimental data of the undamaged structure may be required. Rucka and Wilde[22] explore the application of wavelet transform to damage identification. Rucka[24] also investigates the benefits and limitations of considering higher vibrational modes. In these two research papers and in order to reduce the boundary effects, a cubic spline was used, but only to extrapolate additional points from the numerical simulation data. A similar approach was considered by Katunin *et al.*[29], who also stated that the most effective way of signal extension is the cubic spline extrapolation. Solis *et al.*[27] applied cubic splines, but only to reduce the influence of experimental random and local noise and also to obtain additional modal information at interpolation points and thus obtaining clearer information from wavelet analysis. These comprise some of the various methods proposed, which take advantage of an optimal spatial sampling for the use of finite differences or the noise filtering properties of the continuous wavelet transform.

This paper presents a new method for damage identification, which takes advantage of the smoothing properties of cubic spline interpolation. A cubic spline is a function defined in a piecewise manner by third order polynomials such that continuity of the function itself and its derivatives up to the second order is ensured. On account of this fact, the analytical derivative of each piece of the spline consists of a smoothed approximation of the derivative of the interpolated data, whereas the use of finite differences would yield discontinuities. Furthermore, when computing the derivative using samples of a curve with cubic spline interpolation, all the samples considered influence the computation, whereas only neighbouring samples are considered using finite differences. For the reasons mentioned above, one would expect this technique to have a greater immunity to noise and measurement uncertainty propagation when compared with finite differences, allowing, therefore, for a clearer damage identification. Additionally, an optimal spatial sampling interval is derived as a means of setting the influence of measurement uncertainty and noise propagation to a minimum. This approach is based on the differentiation of modal rotation fields, obtained using shearography, as suggested in Lopes *et. al.*[31], leading to lower noise susceptibility and higher measurement precision.

As stated earlier in this paper, shearography is an optical technique which enables the measurement of the gradient of the displacement fields. Therefore, computing an approximation of the modal curvature shape using the analytical derivative of the interpolating cubic spline of the rotation fields, provided experimentally by shearography, should yield an acceptable immunity level to both noise and measurement uncertainty. It is important to note that if one interpolates the displacement field by a cubic spline, the curvature is obtained by its second derivative and is, thus, only piecewise linear. On the other hand, if one computes the curvature after interpolating the rotation field, the curvature will be defined in a piecewise manner by second order polynomials. Furthermore, there are already portable commercial shearography devices, as we can see in Francis *et al.*[9], which measure the modal rotation field in real-time. In fact, given that after the acquisition the computation of the modal curvature field with the presented method is straight-forward, it is easily implemented in practical cases.

The performance of the present method is assessed using experimental data. Furthermore, small and multiple damage scenarios are explored with special attention, because most of the current methods are not able to deal with such complex cases. On top of that, damage localisation and relative quantification is performed using two different damage factor schemes, combining all the available modes. The first scheme is defined by the difference between damaged and undamaged scenarios and the second is based on a baseline-free approach. This last scheme, based on optimal spatial sampling of a cubic spline interpolation and a robust Fourier fitting, leads to the best results. The performance achieved by the method put forward in this paper is also compared tothe performance obtained using finite differences. This comparison is carried out by computing a damage localisation quality index. The results obtained with the proposed damage identification method reveal the potential and flexibility to be extended to plates and tridimensional structures. However, this analysis is not undergone herein, given that this paper focus on the derivation of the optimal sampling interval and its proof of concept, whose careful analysis is required as we are dealing with a novel approach to damage identification.

This paper is organized as follows. In Section 2, a theoretical analysis is conducted, addressing basic definitions, as well as concepts involved, such as the type of matrices one obtains in the formulation of cubic splines. In Section 3, the method of damage localisation and relative quantification using cubic spline interpolation is adressed. The results of the application of said technique are presented and discussed on Section 4. Finally, Section 5 presents the main conclusions of this paper.

2 | THEORETICAL ANALYSIS OF CUBIC SPLINE INTERPOLATION

In this section, a theoretical analysis is conducted, addressing basic definitions, as well as concepts involved, such as the type of matrices one obtains in the formulation of cubic splines.

The formal definition of a cubic spline is as follows: given a one-dimensional mesh, $\Gamma = \{x_0, \dots, x_n\}$, with $x_0 < x_1 < \cdots < x_n$, a function $s : [x_0, x_n] \to \mathbb{R}$ is said to be a cubic spline which interpolates the points $(x_0, y_0), \dots, (x_n, y_n)$, if the following conditions are met:

1. $s \in C^2[x_0, x_n]$;
2. for $x \in [x_{i-1}, x_i]$, $i = 1, 2, \dots, n$, s is a third degree polynomial;
3. $s(x_i) = y_i,\ i = 0, 1, \dots, n$,

where the differentiability class C^2 is, by definition, the class of continuous functions whose derivatives, up to the second order, exist and are also continuous.

To define an interpolating spline of the points $(x_0, y_0), \dots, (x_n, y_n)$, one starts by constraining the continuity of its second derivative, given in Lagrange's form by

$$s'' = m_{i-1}\frac{x_i - x}{h_i} + m_i\frac{x - x_{i-1}}{h_i}\,, \tag{1}$$

for $x \in [x_{i-1}, x_i]$, where $h_i = x_i - x_{i-1}$ and m_i is the second derivative of the spline function evaluated in node x_i.

Integrating equation (1) twice and constraining the continuity of the spline by setting

$$\begin{aligned} s(x_{i-1}) &= y_{i-1} \\ s(x_i) &= y_i \end{aligned} \tag{2}$$

yields, for $x \in [x_i, x_{i-1}]$

$$s = m_{i-1}\frac{(x_i - x)^3}{6h_i} + m_i\frac{(x - x_{i-1})^3}{6h_i} + \left(y_{i-1} - m_{i-1}\frac{h_i^2}{6}\right)\frac{x_i - x}{h_i} + \left(y_i - m_i\frac{h_i^2}{6}\right)\frac{x - x_{i-1}}{h_i}\,. \tag{3}$$

Differentiating equation (3) one gets

$$s' = -m_{i-1}\frac{(x_i - x)^2}{2h_i} + m_i\frac{(x - x_{i-1})^2}{2h_i} + \frac{y_i - y_{i-1}}{h_i} - (m_i - m_{i-1})\frac{h_i}{6} \tag{4}$$

and constraining its continuity one obtains the identity

$$m_{i-1}\frac{h_i}{6} + m_i\frac{h_i + h_{i+1}}{3} + m_{i+1}\frac{h_{i+1}}{6} = \frac{y_{i+1} - y_i}{h_{i+1}} - \frac{y_i - y_{i-1}}{h_i}\,, \tag{5}$$

for $i = 1, \dots, n-1$, which, for the particular case of uniform spacing, h , is given by

$$m_{i-1} + 4m_i + m_{i+1} = \frac{6}{h^2}(y_{i+1} - 2y_i + y_{i-1})\,. \tag{6}$$

Given a dataset one may compute an approximation of the derivative of the corresponding sampled function as the derivative of the interpolating spline, given by equation (4), once $m_0, \dots, m_n$ are determined. To compute these constants one must make use of equations (5) or (6), if we have a uniform spacing, which define a set of $n-1$ linear equations. Since we have $n+1$ unknowns m_i, two additional restrictions, the so-called boundary conditions, ought to be imposed. Provided that a large number of samples are taken of the rotation of the beam, the effect of the boundary conditions is limited to its edges, therefore, for the sake of simplicity, the following analysis is undergone considering the constraints

$$\begin{aligned} m_0 &= 0 \\ m_n &= 0\,, \end{aligned} \tag{7}$$

resulting in what is known as a natural spline. It is, thus, possible to write the system of linear equations to determine the second derivative of interpolating spline evaluated at the inner nodes, $m_1, \dots, m_{n-1}$, assuming uniform spacing h, in compact form as

$$\mathbf{A}\mathbf{m} = \mathbf{b}\,, \tag{8}$$

which, in expanded form, is written as

$$\begin{bmatrix} 4 & 1 & & & 0 \\ 1 & 4 & \ddots & & \\ & \ddots & \ddots & \ddots & \\ & & \ddots & 4 & 1 \\ 0 & & & 1 & 4 \end{bmatrix} \begin{bmatrix} m_1 \\ m_2 \\ \vdots \\ m_{n-2} \\ m_{n-1} \end{bmatrix} = \begin{bmatrix} 6\left(y_2 - 2y_1 + y_0\right)/h^2 \\ 6\left(y_3 - 2y_2 + y_1\right)/h^2 \\ \vdots \\ 6\left(y_{n-1} - 2y_{n-2} + y_{n-3}\right)/h^2 \\ 6\left(y_n - 2y_{n-1} + y_{n-2}\right)/h^2 \end{bmatrix}. \tag{9}$$

It is particularly interesting to note that matrix **A** in equation (8) is a symmetric positive definite and diagonally dominant tridiagonal matrix. According to Gershgorin circle theorem[32], its spectrum is bounded by $4-|1|-|1|=2$ and $4+|1|+|1|=6$. Since matrix **A** is also a normal matrix, its condition number is upper bounded by 3 as $n \to \infty$. For these reasons, the system of equations in (8) can be solved using the Thomas algorithm[33], allowing, therefore, for a very efficient method of determining **m**. Furthermore matrix **A**, in equation (8), is a square symmetric tridiagonal Toeplitz matrix, whose properties are necessary to model the propagation of errors. These properties are presented in what follows and consist of particularised results obtained by Yueh[34].

Let **T** be a $n \times n$ tridiagonal Toeplitz matrix of the form

$$\mathbf{T} = \begin{bmatrix} b & a & & 0 \\ a & \ddots & \ddots & \\ & \ddots & \ddots & a \\ 0 & & a & b \end{bmatrix} : \tag{10}$$

1. **T** has n distinct eigenvalues given explicitly by

$$\lambda_k = b + 2|a| \cos \frac{k\pi}{n+1}, \; k = 1, \dots, n \, ; \tag{11}$$

2. The eigenvector $\mathbf{v}^{(k)} = [v_1^{(k)}, \dots, v_n^{(k)}]^\top$, corresponding to eigenvalue λ_k, can also be written explicitly as

$$v_j^{(k)} = \sin \frac{kj\pi}{n+1}, \; j = 1, \dots, n \, . \tag{12}$$

3 | DAMAGE LOCALISATION AND RELATIVE QUANTIFICATION METHOD

Applying spline interpolation, described in the previous section, to the modal rotation field, a quadratic approximation of the curvature field is obtained. Conversely, using the displacement field, one would have to differentiate the interpolating spline twice resulting in a linear approximation of the curvature field. In other words, whereas in the latter case one makes use of equation (1), which is the approach followed in this paper, in the former equation (4) is applied.

3.1 | Optimal spatial sampling interval

In any damage identification method there are two kinds of errors: (i) the error of the numerical technique used and (ii) the propagation of noise and measurement uncertainty. The goal of this analysis is to seek an optimal uniform spatial sampling interval, which minimises the combined effect of the propagation of such errors. Such optimal spacing should reject oscillations given by the errors that are intrinsic to the experimental procedure, allowing, simultaneously, small perturbations to the curvature of the beam at the damaged zone to be identified.

First, the error induced by approximating the modal curvature field, of mode q at a point x^* by the derivative of the cubic spline which interpolates uniformly samples of the modal rotation field without any noise contamination, denoted herein as $\tilde{\theta}_q(x)$ is bounded by[35,36]

$$|E_q^{(m)}(x^*)| \leq \frac{1}{24} \left| \frac{\partial^4 \tilde{\theta}_q(x)}{\partial x^4} \right|_\infty h^3 \, , \tag{13}$$

where h is the uniform sampling interval. Although this expression suggests a global dependence of the error, for small grids and smooth functions, as the case being explored, it is a valid approach to define the error locally[37]. Furthermore, the constant $1/24$ is proven to be optimal[38] and, thus, it is valid to consider the following approximation:

$$|E_q^{(m)}(x^*)| \approx \frac{1}{24} \left| \frac{\partial^4 \tilde{\theta}_q(x^*)}{\partial x^4} \right| h^3 \, . \tag{14}$$

It is important to remark that the error of the method itself increases proportionally to the third power of h.

Second, samples of $\tilde{\theta}_q(x)$, given by $\breve{\theta}_q(x)$, are contaminated with error associated with noise and measurement uncertainty, $E_q^{(u)}$, defined for a point x^* and mode q as

$$\tilde{\theta}_q(x^*) = \breve{\theta}_q(x^*) + E_q^{(u)}(x^*) \, . \tag{15}$$

To model this error, one may set a bound to its absolute value. It is noticeable, from the error analyses presented in Zastavnik *et al.*[39] and Lopes *et al.*[40], that the noise and measurement uncertainty reach large values in maximum amplitudes of the modal rotations or its vicinity, whereas it is negligible in amplitudes close to zero, suggesting an approximately linear dependence. Although there is no physical principle that indicates such linear dependence, it is, herein, shown that it is a good approximation for experimental results, yielding good results. For these reasons, and defining ϵ as the relative precision of the smoothed modal rotation field measurements, $E_q^{(u)}$ is modelled herein as

$$|E_q^{(u)}(x^*)| \leq \epsilon \, |\breve{\theta}_q(x^*)| \, , \tag{16}$$

where ϵ is estimated to be the standard deviation of the normalised rotation field profiles after having been smoothed for different experimental samples. The smoothing scheme used consisted in applying a least-squares cubic B-spline filter to the experimental data[8]. The analysis of the error propagation is treated statistically and is carried out under the assumption that noise and measurement uncertainty for different samples are uncorrelated. Furthermore, provided that the objective of this derivation is to find an optimal spatial sampling interval to remove irregularities in the curvature field profile due to the amplification of errors, throughout this derivation the error in the samples to be considered is the maximum given by equation (16).

Considering the system of linear equations (8) used to compute the second derivative of the interpolating spline, which needs to be evaluated at each node, one can see that the components of vector $\mathbf{b}$ are written as

$$b_i = \frac{6}{h^2} \left(\tilde{\theta}_q(x_{i+1}) - 2\tilde{\theta}_q(x_i) + \tilde{\theta}_q(x_{i-1}) \right) \, , \tag{17}$$

whenever the samples of the rotation field are contaminated with errors. Accounting for the propagation of errors in accordance to equation (15) the absolute error in vector $\mathbf{b}$, represented by $\delta\mathbf{b}$, has its components given by

$$\delta b_i = \frac{6}{h^2} \left(E_q^{(u)}(x_{i+1}) - 2E_q^{(u)}(x_i) + E_q^{(u)}(x_{i-1}) \right) \, . \tag{18}$$

Taking into consideration equation (16) and the assumptions initially made, the absolute value of the components of $\delta\mathbf{b}$ is approximated as

$$\begin{aligned} |\delta b_i| &\approx \sqrt{\left(\frac{6}{h^2}\right)^2 \left(\epsilon|\breve{\theta}_q(x)|\right)^2 + \left(\frac{12}{h^2}\right)^2 \left(\epsilon|\breve{\theta}_q(x)|\right)^2 + \left(\frac{6}{h^2}\right)^2 \left(\epsilon|\breve{\theta}_q(x)|\right)^2} \\ &\approx \frac{6\sqrt{6}\,\epsilon}{h^2} |\breve{\theta}_q(x)| \, . \end{aligned} \tag{19}$$

This expression can be used to establish a relation between $\delta\mathbf{b}$ and the error propagated to vector $\mathbf{m}$, denoted as $\delta\mathbf{m}$. Considering the errors $\delta\mathbf{b}$ and $\delta\mathbf{m}$, equation (8) is rewritten as

$$\mathbf{A}(\mathbf{m} + \delta\mathbf{m}) = \mathbf{b} + \delta\mathbf{b} \tag{20}$$

and thus

$$\mathbf{A}\,\delta\mathbf{m} = \delta\mathbf{b} \, . \tag{21}$$

It is fundamental to remark that $\mathbf{A}$ is a square symmetric tridiagonal Toeplitz matrix, of the form in equation (10). As it is apparent from the properties of this type of matrices, namely the one described by equation (11), all eigenvalues of $\mathbf{A}$ are non-null, therefore $\mathbf{A}$ is invertible and equation (21) can be written as

$$\delta\mathbf{m} = \mathbf{A}^{-1}\delta\mathbf{b} \, . \tag{22}$$

Furthermore, $\mathbf{A}$ is diagonalizable and has distinct eigenvalues. Given this fact, one can perform an eigendecomposition and write $\mathbf{A} = \mathbf{V}\mathbf{D}\mathbf{V}^\top$, where $\mathbf{V}$ is a $n \times n$ matrix whose kth column corresponds to the normalised eigenvector $\mathbf{v}^{(k)}$ given by equation (12); $\mathbf{D}$ is a $n \times n$ diagonal matrix whose diagonal entries are the eigenvalues of $\mathbf{A}$, *i.e.* $D_{kk} = \lambda_k$ given by equation (11). Making use of such factorisation, the inverse of $\mathbf{A}$ is written as

$$A_{ij}^{-1} = V_{ik} D_{kl}^{-1} V_{lj} \, , \tag{23}$$

where

$$D_{kl}^{-1} = \frac{1}{\lambda_k} \delta_{kl} \, , \tag{24}$$

being δ_{kl} the Kronecker delta and λ_k are the eigenvalues of $\mathbf{A}$. Rewriting equation (23) and substituting in equation (22) yields

$$\delta m_i = \frac{V_{ik} V_{kj}}{\lambda_k} \delta b_j \, . \tag{25}$$

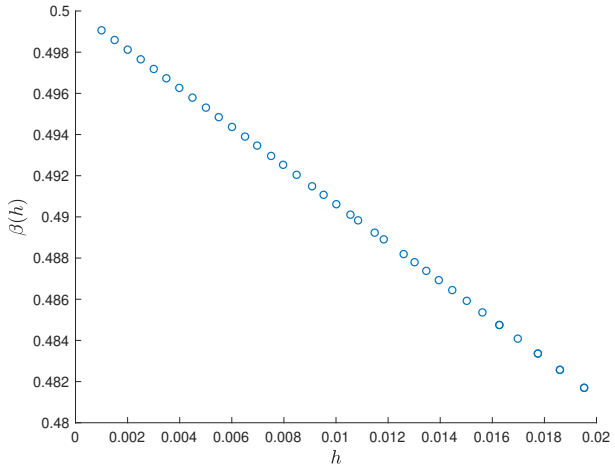

FIGURE 1 Variation of β with h

From the definition of the inverse of a matrix, one can see that the diagonal entries of the inverse of a tridiagonal matrix are dominant over the remaining entries. This fact suggests, as expected, a strong dependence of the ith component of $\delta\mathbf{m}$ on the ith component of $\delta\mathbf{b}$. It is, therefore, valid, considering the assumptions made on the error model, to write

$$|\delta m_i| \approx \beta(h)|\delta b_i| \,, \tag{26}$$

where $\beta(h)$ is defined as

$$\beta(h) = \frac{1}{n}\sum_{i=1}^{n}\left(\sum_{j=1}^{n}\sum_{k=1}^{n}\left|\frac{V_{ik}V_{kj}}{\lambda_k}\right|\right) , \tag{27}$$

in the sense that it is the average sum of the error weights. Taking into consideration the dominance of the diagonal entries, by the definition above, it is clear that β varies proportionally with $1/h$, since $n \propto 1/h$. Furthermore, since values of h with meaning are very close to zero one approximates $\beta(h)$ by a linear relation around zero, which yields

$$\beta(h) = \beta_0 + \beta_1 h \,, \tag{28}$$

where $\beta_0, \beta_1 \in \mathbb{R}$.

For these reasons, substituting equation (19) in equation (26) it is possible to write

$$|\delta m_i| \approx \frac{6\sqrt{6}\beta_0\epsilon}{h^2}|\breve{\theta}_q(x)| + \frac{6\sqrt{6}\beta_1\epsilon}{h}|\breve{\theta}_q(x)| \,. \tag{29}$$

Fig. 1 shows the the dependence of β with h, which not only validates the linear approximation around zero, but also indicates that both β_0 and β_1 are of the same order of magnitude. Given this fact, for values of h around zero, the second term in equation (29) is negligible, yielding

$$|\delta m_i| \approx \frac{6\sqrt{6}\beta_0\epsilon}{h^2}|\breve{\theta}_q(x)| \,. \tag{30}$$

The analytical derivative of the cubic spline is given by equation (4), which applied to the rotation field data yields a quadratic polynomial given by

$$\frac{\partial\tilde{\theta}_q(x^*)}{\partial x} \approx -m_{i-1}\frac{(x_i - x^*)^2}{2h} + m_i\frac{(x^* - x_{i-1})^2}{2h} + \frac{\breve{\theta}_q(x_i) - \breve{\theta}_q(x_{i-1})}{h} - (m_i - m_{i-1})\frac{h}{6} \,, \tag{31}$$

for $x^* \in [x_{i-1}, x_i]$. It is visible, in the expression above, that, for a given experimental data interpolation caracterized by constant moments m_i, the propagated error is maximum at either of the nodes. This way, instead of considering the propagated error of a given interpolation for every spatial position x^*, the spatially maximum error is considered. Given the fact that the goal is to minimise the oscillations in the entirety of the curvature graph, one must take this into account and, thus, consider the minimisation of such error amplification for the points in which it is more likely to occur, *i.e.*, the nodes. It is particularly important to do this analysis for this expression, as if one takes the mean of the error instead, the propagation of the error related

to the second derivative at each node would cancel out. This result would certainly lead to unwanted oscillations. As a result, the induced error, $E_q^{(p)}(x^*)$, is considered to be the maximum, which is attained at either of the nodes, and given by

$$\begin{aligned} E_q^{(p)}(x^*) &\approx -\delta m_{i-1}\frac{h}{2} + \frac{E_q^{(u)}(x_i)}{h} - \frac{E_q^{(u)}(x_{i-1})}{h} - \delta m_i\frac{h}{6} + \delta m_{i-1}\frac{h}{6} \\ &\approx -\delta m_{i-1}\frac{h}{3} - \delta m_i\frac{h}{6} + \frac{E_q^{(u)}(x_i)}{h} - \frac{E_q^{(u)}(x_{i-1})}{h}\,. \end{aligned} \tag{32}$$

Neglecting correlations between errors and considering equations (16) and (30)

$$\begin{aligned} |E_q^{(p)}(x^*)| &\approx \sqrt{\left(\left(\frac{h}{3}\right)^2 + \left(\frac{h}{6}\right)^2\right)\left(\frac{6\sqrt{6}\beta_0\epsilon}{h^2}|\breve{\theta}_q(x^*)|\right)^2 + 2\left(\frac{1}{h}\right)^2\left(\epsilon|\breve{\theta}_q(x^*)|\right)^2} \\ &\approx \frac{\epsilon|\breve{\theta}_q(x^*)|}{h}\gamma\,, \end{aligned} \tag{33}$$

with γ defined as

$$\gamma = \sqrt{30\beta_0^2 + 2}\,. \tag{34}$$

It is important to note that the error concerning the propagation of the measurement uncertainty is inversely proportional to h.

Considering equations (14) and (33), the total error is, approximately, given by

$$|E_q^{(t)}(x)| \approx \frac{1}{24}\left|\frac{\partial^4\tilde{\theta}_q(x)}{\partial x^4}\right|h^3 + \frac{\epsilon|\breve{\theta}_q(x)|}{h}\gamma\,. \tag{35}$$

Taking into account that the two kinds of error behave differently in relation to h, it is possible to determine $h_q^{(opt)}$ such that the expression above is minimised. Taking the derivative in relation to h of the expression above and equaling it to zero yields

$$h_q^{(opt)} = \left(8\epsilon\gamma\frac{|\breve{\theta}_q(x)|}{\left|\frac{\partial^4\tilde{\theta}_q(x)}{\partial x^4}\right|}\right)^{1/4}\,. \tag{36}$$

It is interesting to note that the expression above suggests the error varies with x. However, as it will be discussed in the next section, $|\breve{\theta}_q(x)|/\left|\frac{\partial^4\tilde{\theta}_q(x)}{\partial x^4}\right|$ is approximately constant in the interval considered. As a result, one can take the mean of the quotient in question yielding

$$h_q^{(opt)} = \left(8\epsilon\gamma\left\langle\frac{|\theta_q(x)|}{\left|\frac{\partial^4\theta_q(x)}{\partial x^4}\right|}\right\rangle\right)^{1/4}\,, \tag{37}$$

where numerical simulation values for the undamaged scenario are used.

3.2 | Factors for damage localisation

Following a similar approach as the one in Abdel Wahab *et al.*[11] and Mininni *et al.*[8] it is possible to make use of the data of the structure in an undamaged scenario to detect and make a prediction on the location of damage present in the structure. Indeed, the difference between the curvature profiles for the undamaged and damage scenarios should yield a good indicator of its location. As a matter of fact, the modified curvature damage factor is defined as[8]

$$\mathrm{MCDF}(x) = \frac{1}{N}\sum_{q=1}^{N}\left|\frac{\partial\tilde{\theta}_q(x)}{\partial x} - \frac{\partial\theta_q(x)}{\partial x}\right|\,, \tag{38}$$

where N is the number of experimentally measured modes. The use of this factor is a way of combining the contribution of all the modes available, and thus of summing the damage signatures. However, it requires that data of the undamaged condition has been previously measured. Often, especially for older structures, such data may have not been collected and thus it is not available. Therefore, a baseline-free alternative must be sought. In view of this problem, instead of using the curvature field of the undamaged structure as a comparison, one may use a profile that robustly fits the damaged curvature field. The fundamental concept behind such approach is that a robust fit, in the sense that outliers are rejected, of the curvature field of the damaged structure preserves the smoothness of its undamaged areas, neglecting, simultaneously, the damage signatures,

which are regarded as outliers. Selecting an appropriate model, in the areas identified as outliers, the fitted curve will consist of a smooth extension of the undamaged curvature profile. For these reasons, the difference between these profiles should yield good performance as far as detecting abnormalities in the modal curvature profile of a structure is concerned. Nevertheless, this scheme is very sensitive to perturbations, since it relies on a robust fit, meaning that measurement and noise error wrongfully flag damage on the structure. Given this fact, the use of an optimal spatial sampling, as a means of mitigating the effect of such errors, is necessary.

Knowing the present problem relies on a vibrational analysis of a structure one may take advantage of its periodic properties for the construction of the fitness model. On account of that, a fitness model based on the Fourier Series is also put forward in this paper, given that it is guaranteed to converge and it is composed of periodic functions. This model is designated herein as adjusted curvature damage factor, ACDF, and is defined as

$$\mathrm{ACDF}(x) = \frac{1}{N}\sum_{q=1}^{N}\left|\frac{\partial\tilde{\theta}_q(x)}{\partial x} - \mathcal{F}^{(m)}(x)\right| , \tag{39}$$

where $\mathcal{F}^{(m)}(x)$ is the robust fit of $\partial\tilde{\theta}_q(x)/\partial x$ using a partial Fourier series expansion with m terms, *i.e.* a finite sum of the form

$$\mathcal{F}^{(m)}(x) = \frac{a_0}{2} + \sum_{k=1}^{m}\left\{a_k\cos(k\omega\, x) + b_k\sin(k\omega\, x)\right\} , \tag{40}$$

where a_k and b_k are the coefficients of the Fourier series. It is important to remark that if one sets a large value for m, the curvature damage signatures are no longer regarded as outliers. Conversely, a small value leads to the incapacity of the model to fit the curvature profile of the structure.

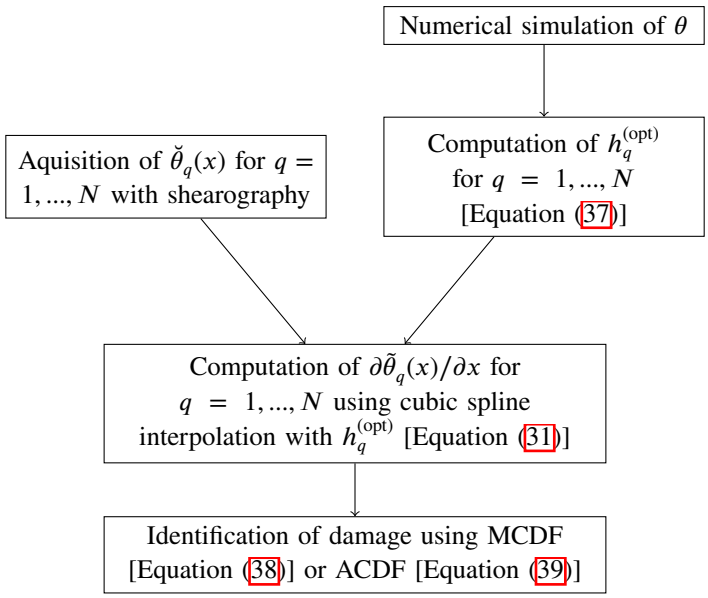

FIGURE 2 Flowchart of the proposed approach for damage identification.

The approach described in this section is schematically represented in Fig. 2. This approach is validated and the performance of both damage factors is assessed and compared in the next section. Furthermore, the dependence of damage size on the significance of the signature obtained with this method is also explored, as a means of relative quantification.

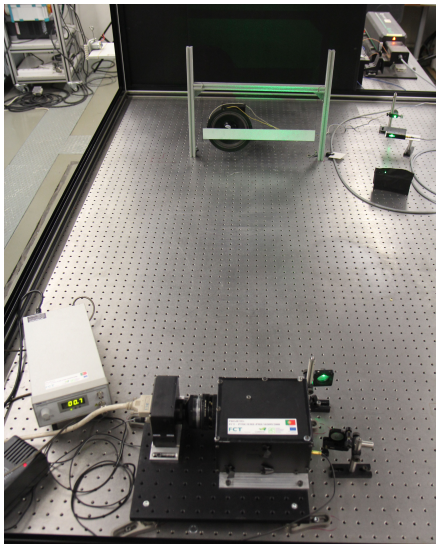

FIGURE 3 Experimental apparatus used.

3.3 | Index for damage localisation quality

To allow for a quantification of the damage localisation quality, an index, inspired in a similar one presented in Moreno-García *et al.*[16], is introduced, as follows

$$\mu = 1 - \frac{\sum_{i=1}^{N_p} \hat{DF}(x_i)}{N_p}, \tag{41}$$

in which $\hat{DF}$ is the normalised damage factor used, *i.e.* either the MCDF or the ACDF, and x_i with $i \in \{1, ..., N_p\}$, are the points at which the damage factor is computed. The normalised damage factor, $\hat{DF}$, is such that the magnitude of the highest peak is unitary, being adequate to evaluate the quality of single damage scenarios only. This index may be interpreted as the normalized area above the damage factor, which would be unitary for an ideal localisation, *i.e.* a localisation in which the damage factor is zero except for a unitary peak of infinitesimal width, corresponding to the damage. As a result, this index evaluates how far is a localisation from the ideal one, due to the influence of noise and dispersion of the identification, for a given method. The damage localisation quality index in equation (41) is applied in this work to compare the sensitivity of the damage factors presently introduced and also to compare the present approach, based on cubic spline interpolation, with others previously used.

4 | RESULTS AND DISCUSSION

4.1 | Experimental Setup and damage scenarios

As stated in the previous sections, the present method is subjected to a validation, for a broad variety of damage scenarios, using experimental data obtained from shearography. The analysed structure is an aluminium beam suspended by rubber bands at both edges, corresponding to a free-free condition. The natural frequency for each mode depends on the damage scenario being considered, as the stiffness of the beam decreases with the presence of damage. Therefore, to excite the beam at its natural frequency, one has to measure it experimentally, for each damage scenario. In the experimental setup devised, such values were determined by measuring the beam response with a microphone after having excited the beam with an impact hammer. A loudspeaker, emitting a sinusoidal wave, was placed behind the beam to excite it at its natural frequencies, while the modal rotation fields were being measured. The shearography system was placed at 1.2 meters from the suspended beam, allowing for the recording of the phase map of the entirety of the beam, which was afterwards processed applying filtering and unwrapping techniques, which are thoroughly described in Mininni *et al.*[8]. The apparatus used is shown in Fig. 3, which is thoroughly described in Mininni *et al.*[8].

The aluminium beam of dimensions 400 mm × 40 mm × 3 mm, which was tested under different damage scenarios. The damage scenarios inflicted to the beam were created using an electronically controlled milling machine, which carved slots of

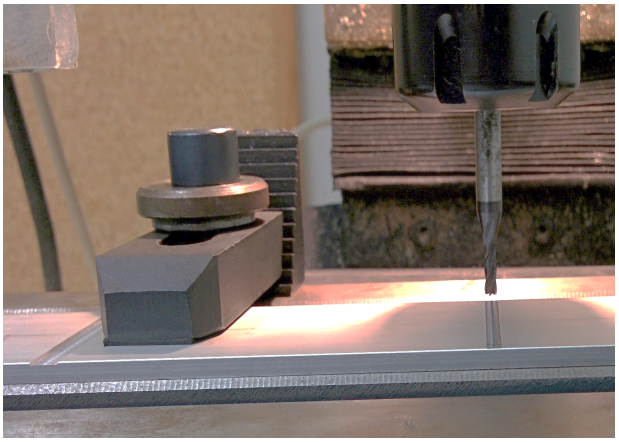

FIGURE 4 Zoomed-in view of the specimen with the two slots.

a certain width and depth, with a 5 micrometer precision. Furthermore, the slots were created in two distinct locations and for several depths, as a means of testing the damage identification method viability for a wide range of situations. Measurements have also been taken on the undamaged beam, followed by increasingly deeper slots at one location and finally, multiple damage scenarios, in which increasingly deeper slots are carved in the second location, while leaving the first constant. The depth of each slot is measured in different points, after the milling process, and averaged. Slot 1 had a width of 5 mm and slot 2 a width of 3 mm, the depths of the slots corresponding to each damage scenario are presented in Table 2. A zoomed-in view of the specimen with the two slots is shown in Fig. 4 and diagrams for damage scenarios four and eight are presented in Figs. 5 and 6.

After the unwrapping and filtering of the phase maps, the rotation fields for each damage scenario for the first four modes were obtained. It is important to remark that, throughout this paper, the modal rotation field is normalised, such that its maximum amplitude is unitary, allowing for a better comparison between damage scenarios. Profiles of the rotation fields of the undamaged scenario and the fourth damage scenario are represented, respectively, in Figs. 7 and 8. Comparing these two figures, it is very difficult to notice any difference between them, justifying the need to analyse the profile of the curvature instead.

4.2 | Optimal spatial sampling

The relative precision of the modal rotation profiles, ϵ, is estimated to be 5×10^{-5}. Applying a linear regression on the data in Fig. 1 yields $\beta_0 = 0.5000$ and $\beta_1 = -0.9373$. Furthermore, the quotient $|\breve{\theta}_q(x)| / \left|\frac{\partial^4 \bar{\theta}_q(x)}{\partial x^4}\right|$ is, for numerical simulation data of the undamaged case scenario, approximately constant over the length of the beam for each mode, thus it is valid to consider its average instead. Making use of equation (37) it is possible to compute the optimal spatial sampling, $h^{(opt)}$, for each mode, which are listed in Table 3.

TABLE 2 Damage scenarios.

Damage scenarios	Slot 1 Depth [mm]	Slot 2 Depth [mm]
1	0.10	–
2	0.22	–
3	0.30	–
4	0.41	–
5	0.41	0.03
6	0.41	0.10
7	0.41	0.19
8	0.41	0.30

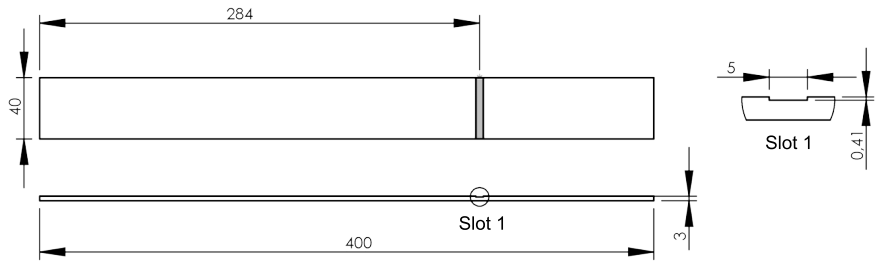

FIGURE 5 Diagram of the beam corresponding to damage scenario four; All dimensions are in mm.

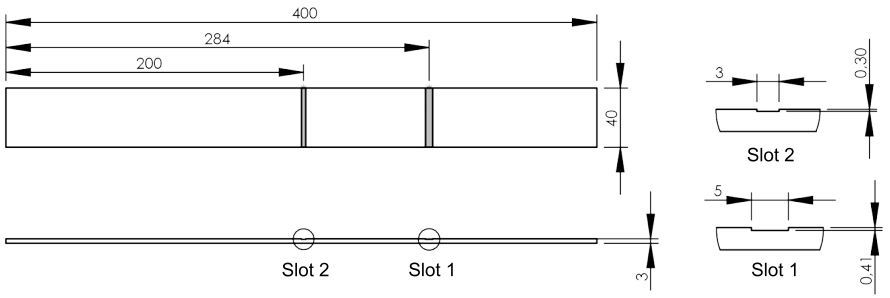

FIGURE 6 Diagram of the beam corresponding to damage scenario eight; All dimensions are in mm.

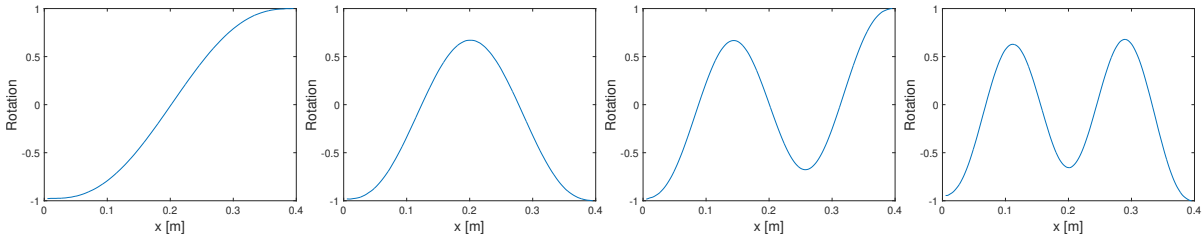

FIGURE 7 Profiles of the rotation fields of the undamaged scenario for the first four modes, respectively, from left to right.

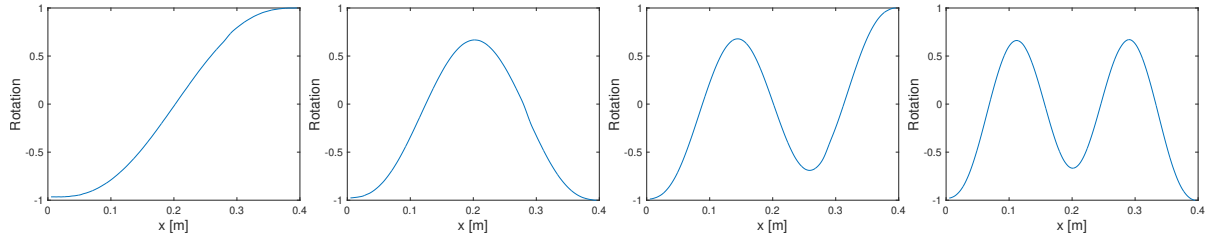

FIGURE 8 Profiles of the rotation fields of the fourth damage scenario for the first four modes, respectively, from left to right.

TABLE 3 Optimal spatial sampling for modes 1, 2, 3 and 4.

Mode	1	2	3	4
$h^{(opt)}$ [mm]	15.85	9.54	6.82	5.30

Some examples of computing the profiles of the curvature by applying cubic spline interpolation are presented in Figs. 9–11 and are subjected to a thorough analysis. As a means of assessing the performance of the optimal spatial sampling scheme, the

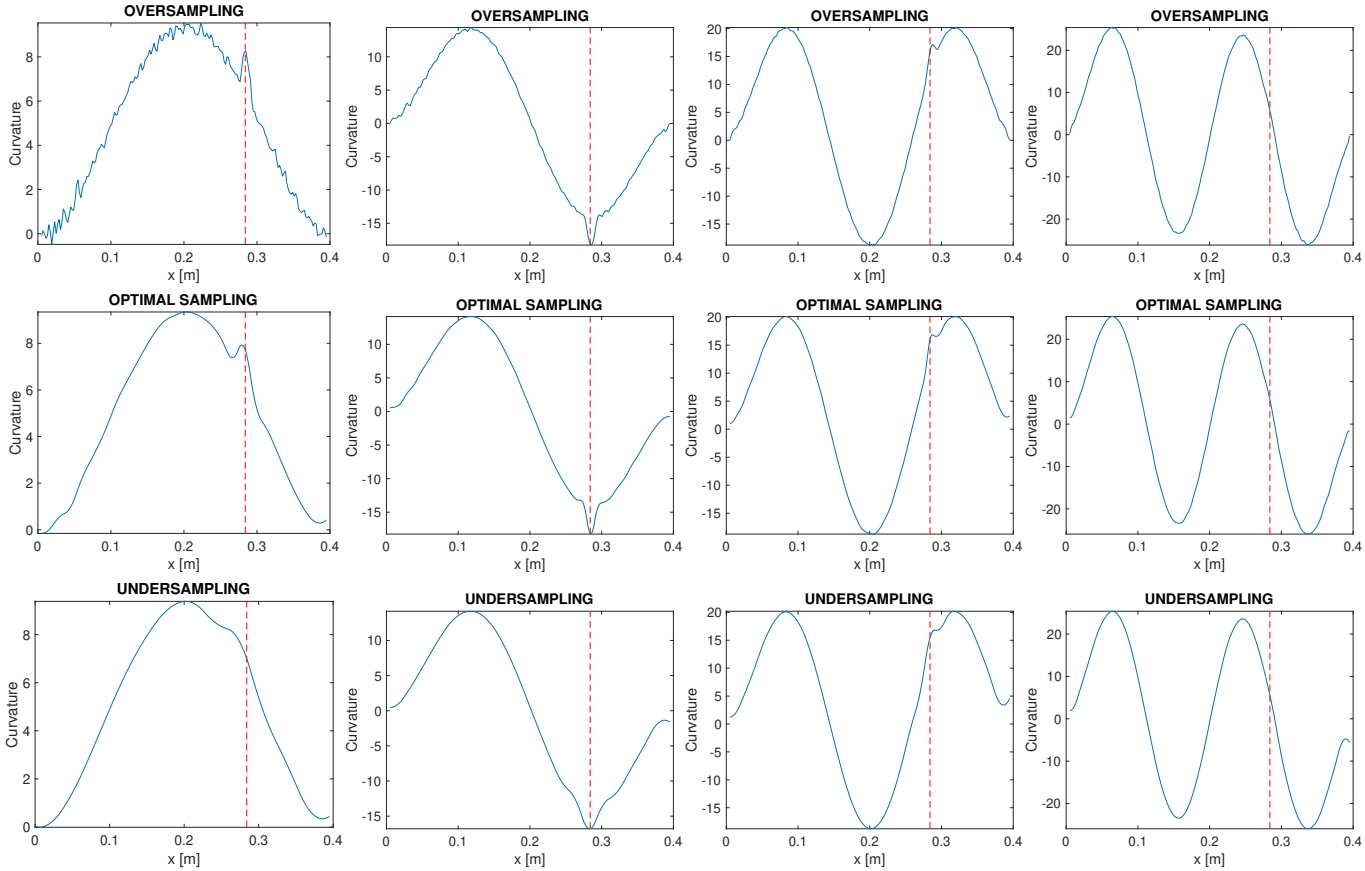

FIGURE 9 Profile of the curvature fields of the fourth damage scenario for modes one to four, respectively from the left to the right columns.

curvature profiles obtained with such optimal interval are compared with undersampling and oversampling situations. Oversampling corresponds to an interval equal to the resolution of the measured rotation profiles, which is, for the data gathered, equal to 0.17 mm and undersampling to an interval which is twice the computed optimal interval.

As a matter of fact, Fig. 9 represents the curvature mode shapes for the most dramatic single damage scenario, *i.e.* damage scenario four, in which a comparison is carried out between the interval derived to be optimum and cases of oversampling and undersampling, for each of the first four modes. Analysing, these plots one can clearly localise a consistent anomaly for the first three modes corresponding to the damage. It is very interesting to point out that, as expected, for small values of the spatial sampling interval the curve is very prone to perturbations caused by noise, and as h increases so does its resistance to those perturbations, having the side effect, however, of smoothing the spike caused by the damage. This clearly indicates the need to select the sampling interval as a means of balancing these effects. Looking at the first row of plots in Fig. 9, corresponding to the oversampling situation, it is clear that for all the modes one sees random perturbations due to noise. On the other hand, setting the sampling interval to the optimum value obtained via the scheme devised, these perturbations are no longer noticeable, yielding a distinct spike in an otherwise smooth curve. This spike, whose location is consistent across the modes, corresponds to the damage inflicted to the beam represented in the plots by a vertical dashed line, validating not only the use of the modal curvature shape as a mean of identifying damage, but also the benefits of using an optimal sampling interval. Furthermore, if one increases the parameter h beyond the optimum interval, the abnormality in the curve due to the damage is significantly reduced, decreasing the quality of the identification, as visible in the last row of plots in Fig. 9.

It is also very interesting to remark that the damage signature is not visible for the fourth mode. In fact, looking at the position of the vertical dashed line, one concludes that it falls in the vicinity of a zero-crossing point of the fourth mode, leading to an inconclusive identification. This fact is one of the drawbacks of using higher vibrational modes, since the higher the mode considered the greater is the number of zero-crossing points, augmenting the likelihood of a damage falling into such regions.

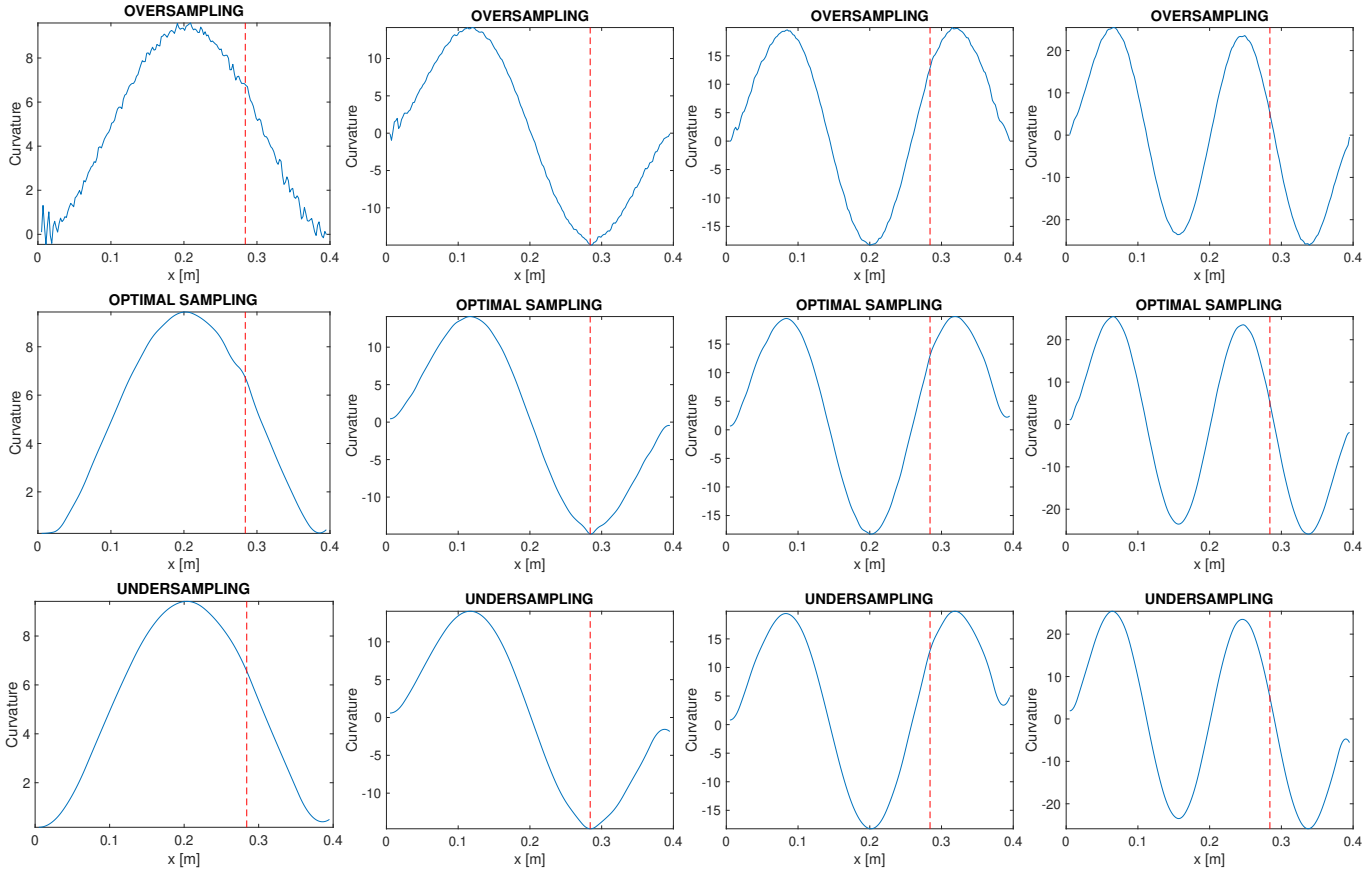

FIGURE 10 Profiles of the curvature fields of the first damage scenario for modes one to four, respectively from the left to the right columns.

Furthermore, it is of great importance to compare the proneness to noise of the different modes. It is noticeable from the analysis of the plots of Fig. 9 that the higher the mode is, the greater the resistance to noise. For instance, for the oversampling situation of first mode the perturbations due to noise are tremendous, but considering higher modes this effect starts to fade, resulting in barely visible oscillations in the curve of the fourth mode. This trait is an advantage of using higher vibration modes, allowing for the use of a smaller sampling interval and therefore considering more data points, which leads to a more marked peak. In other words, for higher vibrational modes the perturbations are eliminated for a smaller sampling interval and, therefore, the damage signature is not as smoothed as in lower modes. Detailed analyses of the noise in shearography measurements are carried out in Zastavnik *et al.*[39] and in Lopes *et al.*[40].

Fig. 10 shows the curvature mode shapes for the smallest single damage scenario, *i.e.* damage scenario one, in which the performance of the optimal spatial sampling is evaluated, for each of the first four modes. This scenario exhibits a considerable challenge to any damage identification method. In fact, the vast majority of the available methods fail to tackle successfully small damage, mainly due to the difficulty of the distinction between noise perturbations and damage signatures, given the similarity in their orders of magnitude. In fact, a technique allowing for such identification should provide for a means of computing the derivative of the modal rotation field in a manner that it takes into account the smoothness of the resulting curve, and simultaneously reducing to a minimum the irregularities resulting of noise and measurement uncertainty. The method presented in this paper was designed to be endowed with such properties. In fact, as depicted in Fig. 10, the use of cubic spline interpolation to the data alongside an optimal choice of the spatial sampling interval successfully identifies the smallest damage. As a matter of fact, considering the plot regarding the optimal interval for the first, second and third modes, one consistently identifies a clear damage signature, which stands out against the smoothness of the curve. Again, as seen in the analysis of Fig. 9, given the location of the damage it is not possible to make any conclusive identification from the plots of the fourth mode. Mininni *et al.*[8] also analysed this damage scenario using finite differences as a means of computing the modal curvature from the rotation

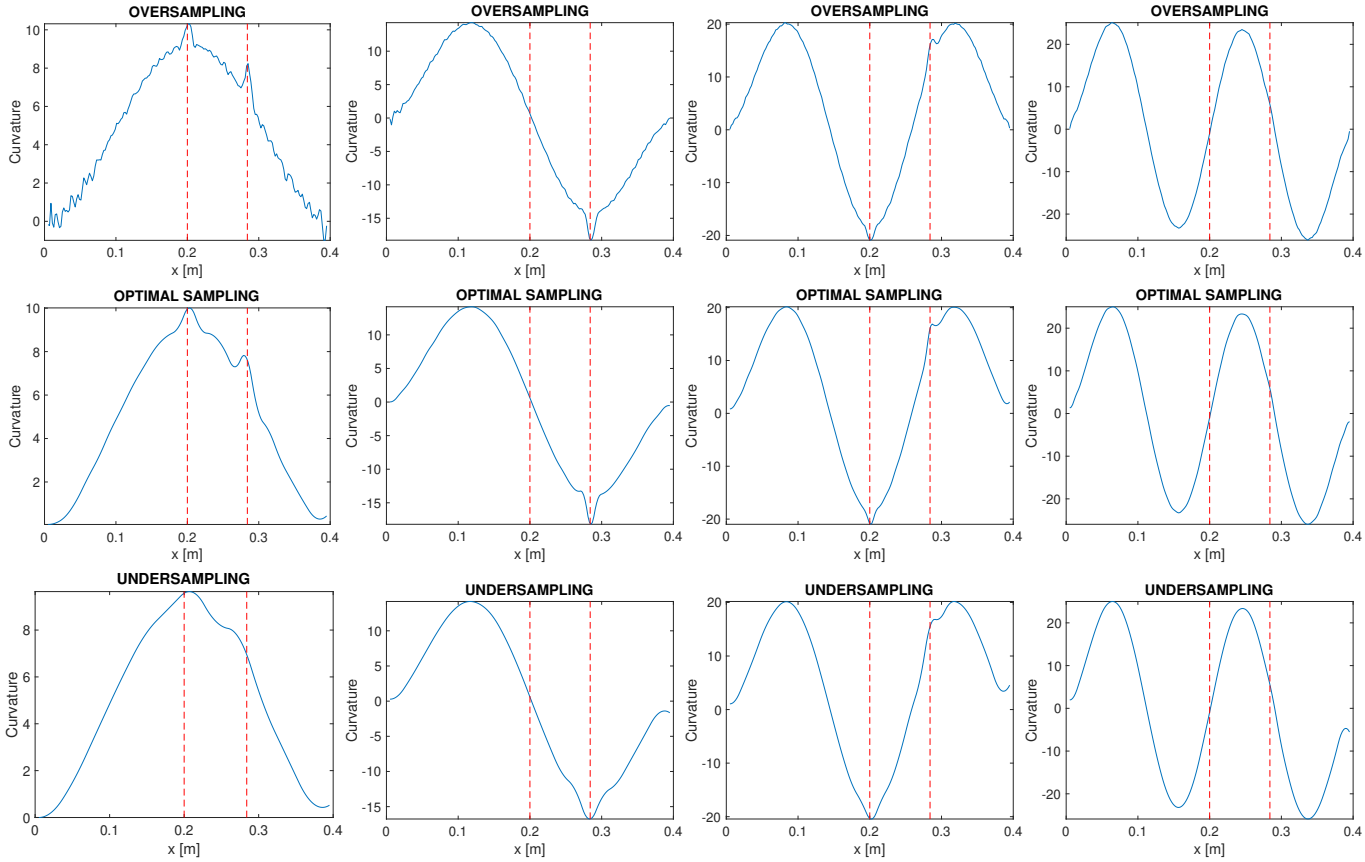

FIGURE 11 Profiles of the curvature fields of the eighth damage scenario for modes one to four, respectively from the left to the right columns.

field of the beam using shearography. Despite the good results obtained overall by the method presented by these researchers, also using an optimal spatial sampling interval, they were not able to identify the first damage scenario, since the perturbation caused by the damage in the curvature is of the same order of magnitude as the oscillations due to noise propagation allowed by the differentiation tool used. Comparing Figs. 9 and 10 one readily notices the consistency of the damage localisation of the present method. Furthermore, it is also visible that the amplitude of the damage signature provides a means of a relative damage quantification, because the abnormality in the curvature increases significantly with the severity of the damage. This result is theoretically expected since a more significant damage locally reduces the stiffness more dramatically and, thus, the dynamic response of the structure.

Fig. 11 represents the curvature mode shapes for the most dramatic multiple damage scenario, *i.e.* damage scenario eight, in which the effectiveness of the optimal spatial sampling in identifying multiple damage is tested. This scenario also poses a challenge to damage identification techniques. However, there are some methods which can achieve this type of identification[8,41,29]. Using an optimal spatial sampling interval, one can clearly notice, analysing Fig. 11, that the method presented in this paper also identifies successfully multiple damage. In fact, the damage corresponding to the first slot is marked with a clear peak on the first three modes. One can also easily spot a distinct damage signature of the second slot for modes one and three. Given that the location of the slots coincides with the zero-crossing vicinity of some modal shapes, it is not possible to identify the first slot in the fourth mode, neither the second slot in the second and fourth modes. Comparing Fig. 11 with Figs. 9 and 10, one can readily conclude that the use of equation (4), which gives the derivative of the cubic spline, is very robust since the damage of the first slot is localised consistently. Furthermore, comparing Figs. 9 and 11 the amplitude of the damage signature is unvarying for the modes where it is localised. For these reasons, the method put forward in this paper shows clear signs of robustness.

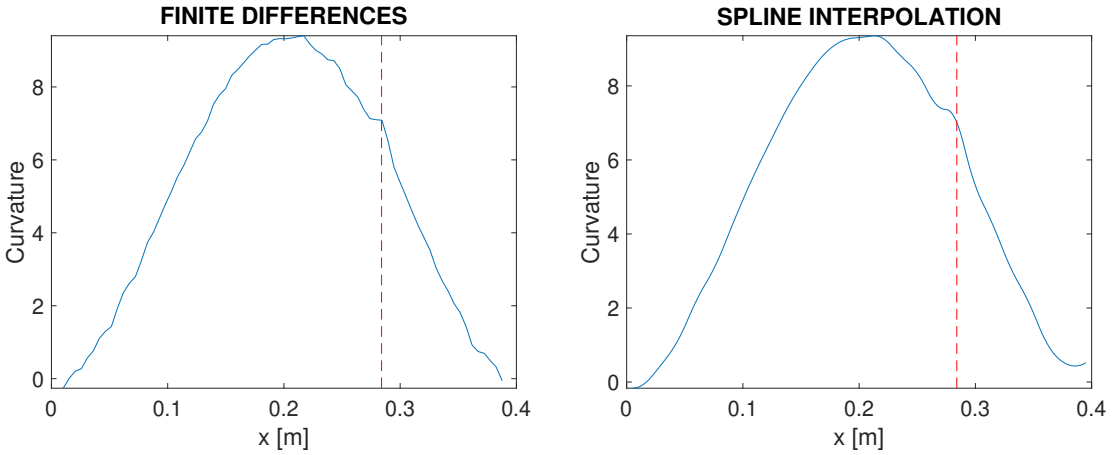

FIGURE 12 Comparison of the curvature profiles of the second damage scenario for the first mode using finite differences and spline interpolation, both with optimal sampling.

It is also worth comparing the results obtained using finite differences with those using cubic spline interpolation. The finite difference in the central point $x^* \in [x_{i-1}, x_i]$ is given by

$$\frac{\partial \tilde{\theta}_q(x^*)}{\partial x} \approx \frac{\breve{\theta}_q(x_{i+1}) - \breve{\theta}_q(x_{i-1})}{2h} \tag{42}$$

where h is the distance from x_{i-1} to x^* and from x^* to x_{i+1}. One can obtain the formula above by differentiating the first order polynomial

$$\tilde{\theta}_q(x^*) \approx \breve{\theta}_q(x_{i-1}) + \breve{\theta}_q[x_{i-1}, x_{i+1}](x^* - x_{i-1}) \tag{43}$$

where $\breve{\theta}_q[x_{i-1}, x_{i+1}]$ is a divided difference. Alternatively, a formulation based on Taylor series expansions can be carried out to obtain (42)[8]. It can be seen that equation (42) is much simpler than equation (31), because it comes from the differentiation of a first order polynomial, instead of a third order polynomial. As a matter of fact, Fig. 12 shows the curvature profiles of the second damage scenario for the first mode using finite differences, with an optimal spatial sampling derived in Mininni *et al.*[8], and using cubic spline interpolation with the optimal sampling interval put forward in this paper. Analysing these plots it is easily perceivable that the use of an optimal spatial sampling interval allied with finite differences is unable to completely remove the oscillations due to noise and measurement uncertainty propagation. On the other hand, the use of cubic spline interpolation proves to be able to remove these oscillations, confirming that the use of the presented technique is endowed with better noise rejection properties. It is also important to remark that the improvement provided by this technique, regarding noise rejection, comes with the advantage of having a sharper damage signature.

4.3 | Damage localisation and relative quantification

In this subsection the values for the MCDF and ACDF are computed for the experimental data gathered, presented previously in this section. The curvature profiles used to obtain these curves are normalised to provide for a better assessment of the quality of the identification. The following damage localisations are obtained considering the optimal sampling interval. Furthermore, a threshold line is also represented in the damage factor plots as a horizontal dashed line, to allow for a better visual discrimination. This threshold is defined as the average of the damage factor plus its standard deviation. As a result, there is a strong indication of the presence of damage only if a peak stands out from the average conditions of the beam.

4.3.1 | Modified Curvature Damage Factor

Fig. 13 shows the MCDF for the single damage scenarios, *i.e.* scenarios one to four, computed using equation (38). Analysing this figure one can clearly notice a distinct peak in all four damage scenarios which corresponds to the carved slot, represented in the plots by a vertical dashed line. It is important to remark that damage was consistently localised, even for the smallest damage inflicted on the beam. However, given the same order of magnitude of the damage signature and the propagated measurement

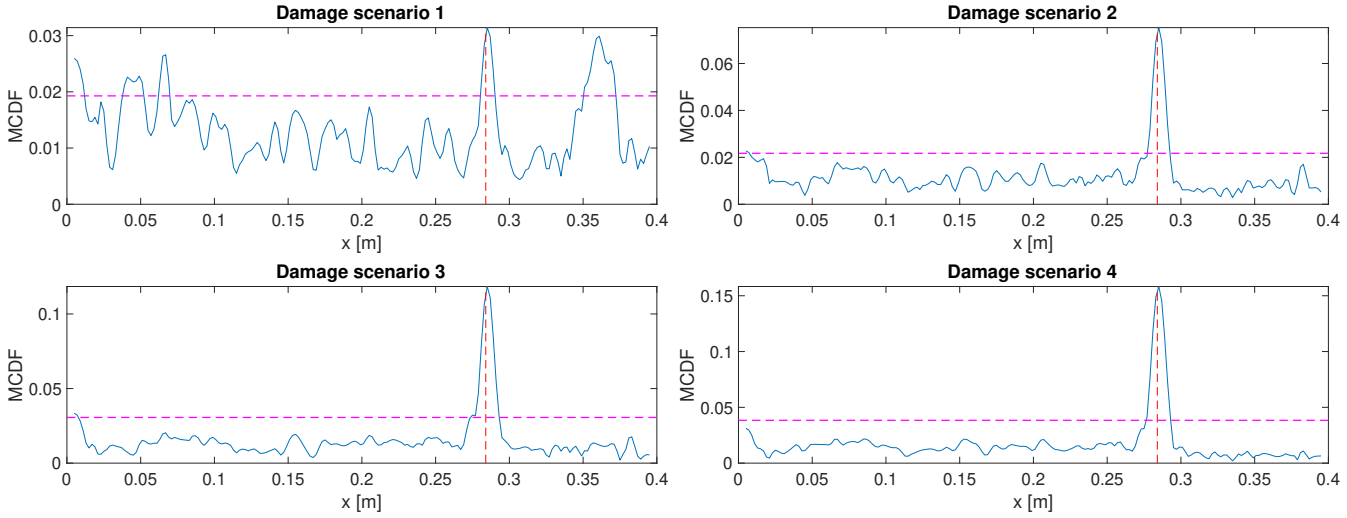

FIGURE 13 MCDF(x) using four modes for the single damage scenarios one to four.

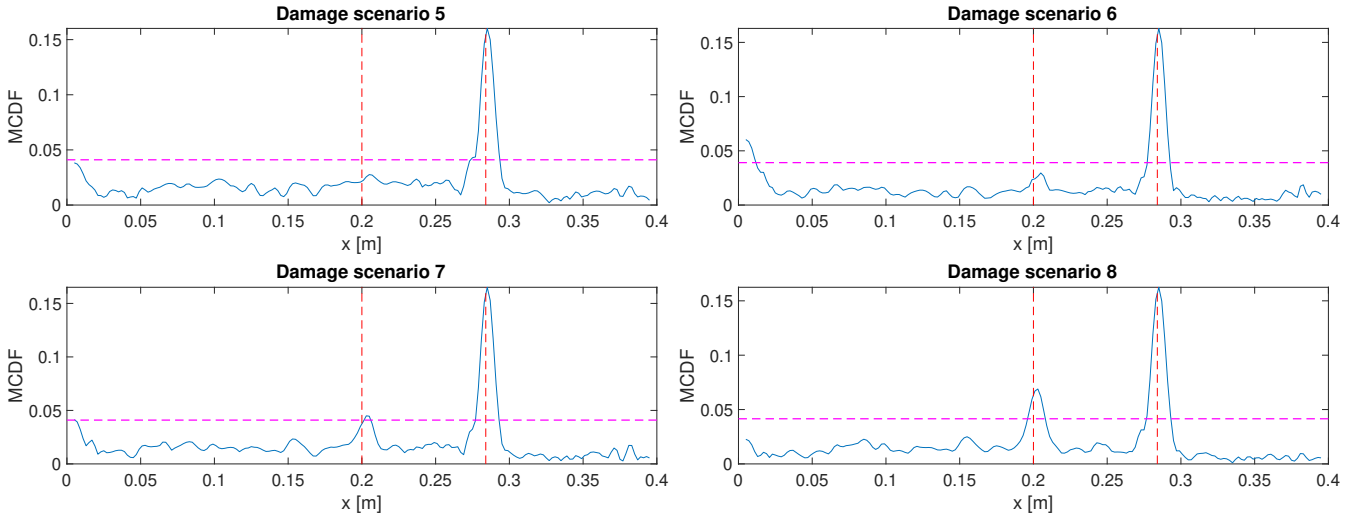

FIGURE 14 MCDF(x) using four modes for the multiple damage scenarios five to eight.

error of the first damage scenario, it is not possible to distinguish between them, resulting in a reduced localisation quality. Nevertheless, for damage scenarios two to four, one can undoubtedly make a distinction between the influence of the propagated error and the presence of damage. It is also interesting to point out that there is a clear dependence of the damage severity on the magnitude of the peak. Moreover, similarly to the curvature plots, the width of the anomaly on the MCDF plots is of a greater order of magnitude when compared with the width of the carved slot.

The computed MCDF for the multiple damage scenarios, *i.e.* scenarios five to eight, is presented in Fig. 14. Looking at the plots of this figure one can see the difficulty in locating very small multiple damage for the fifth scenario. For the sixth to eighth damage scenarios, a small damage is consistently localised corresponding to the second slot carved on the beam. Due to the similarity in magnitude of the propagated measurement errors and the damage signature of the second slot, its localisation is impossible in the fifth scenario. For the sixth and seventh damage scenarios the identification has poor quality, with the damage signature falling below the threshold line. Nevertheless, the present method provides for a clear localisation for the eighth scenario. It is interesting to point out that the magnitude of the peak corresponding to the first slot is very consistent across damage scenarios four to eight, and also that the amplitude of the peak relative to the second slot is an indicator of the size of the damage inflicted.

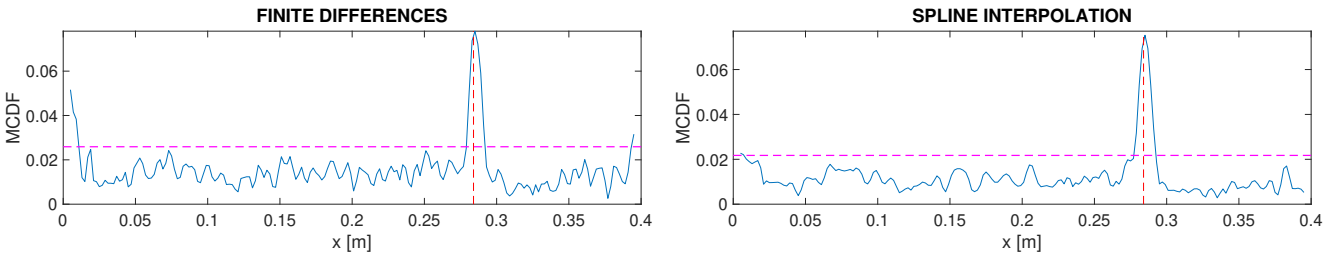

FIGURE 15 Comparison of MCDF(x) using four modes for the second damage scenario with finite differences and cubic spline interpolation.

TABLE 4 Comparison of the damage localisation quality index, μ, for the single damage scenarios.

Damage Scenario	1	2	3	4
Finite Differences (MCDF)	0.5595	0.8028	0.8705	0.8841
Finite Differences (ACDF)	0.7760	0.9197	0.9399	0.9452
Spline Interpolation (MCDF)	0.5844	0.8399	0.8718	0.8925
Spline Interpolation (ACDF)	0.8809	0.9359	0.9439	0.9462

Furthermore, analysing Fig. 15 it is possible to compare the MCDF for the second damage scenario using finite differences and cubic spline interpolation, which corresponds to the smallest damage possible to detect using the MCDF for any of the methods. Inspecting both plots it is noticeable that the use of finite differences is more permeable to noise and measurement uncertainty propagation, while the damage signature of both techniques is very similar as far as both magnitude and distinctness are concerned. First, the damage detection threshold line is lower using the present method, therefore being able to discriminate smaller damage, when compared with a method based on finite differences. Second, Table 4 depicts the damage localisation quality index, computed for both methods. It is clear from its analysis that, using the MCDF, the present approach consistently outperforms the one based on finite differences. The difference between identification qualities is more significant for small damage, when the order of magnitude of the propagated error is similar to the order of magnitude of the damage signatures. Finally, the use of finite differences is also more vulnerable to edge effects, wrongfully flagging damage at the extremity of the beam.

4.3.2 | Adjusted Curvature Damage Factor

Driven by the usual lack of undamaged vibration data of a structure, a baseline-free scheme for damage localisation is also put forward in this paper. Fig. 16 shows the ACDF for single damage scenarios, *i.e.* scenarios one to four, computed using equation (39). The parameter m used to obtain such values was set to 8, which proved adequate for a fit of the first four vibrational modes. Analysing the plots of this figure, it is clear that the influence of the propagated error was significantly reduced, enabling for a very clear and consistent localisation of all single damage scenarios. It is important to point out that the magnitude of the peaks in this figure is very similar to the magnitude of peaks of Fig. 13 for the same scenarios, showing clear signs of robustness. As a matter of fact, unlike ACDF, MCDF uses a baseline which is also subjected to measurement error, therefore it would be expected that the noise yielded by MCDF is inherently larger. For this reason, ACDF provides for a clearer localisation and distinction between propagated error and damage signature, even for small damage.

Fig. 17 shows the ACDF for multiple damage scenarios, *i.e.* scenarios five to eight. This values were computed considering a parameter $m = 8$. Looking at the plots of this figure one can see that a localisation of the second slot is possible for scenarios seven and eight. Indeed, the identification for scenario six is very poor given the reduced dimension of the damage inflicted, whose damage signature falls below the threshold line. When comparing Fig. 17 with Fig. 14, it is interesting to remark that not only is the dimension of the peaks associated with the first slot consistent and very similar, but also that there is a similarity in the magnitude of the signatures corresponding to the second slot, which has slight variations due to the greater error inherent to the MCDF. Table 4 shows the damage localisation index computed with the MCDF and ACDF, for the single damage scenarios.

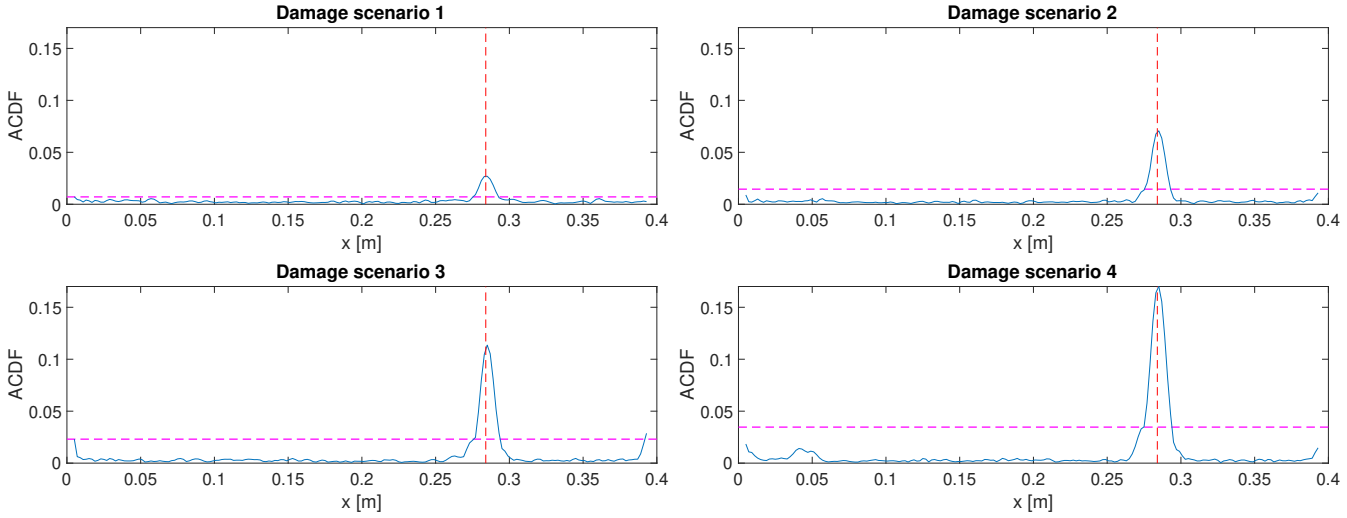

FIGURE 16 ACDF(x) with $m = 8$ using four modes for the single damage scenarios one to four.

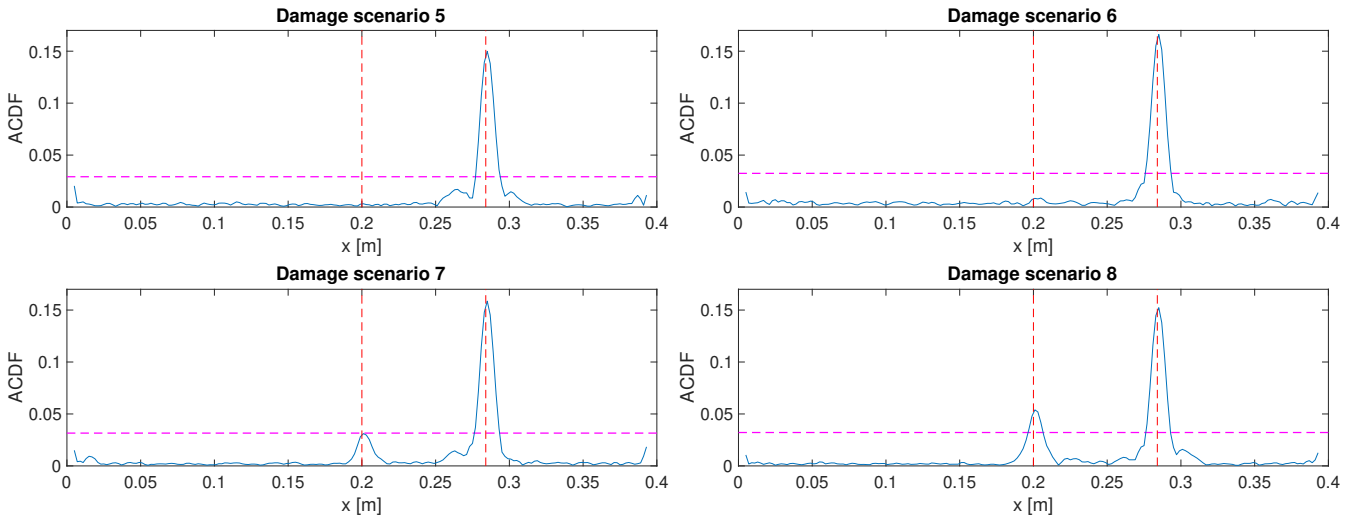

FIGURE 17 ACDF(x) with $m = 8$ using four modes for the multiple damage scenarios five to eight.

It is very clear that the baseline-free damage factor, ACDF, put forward in this paper outperforms, by a considerable margin, the MCDF, which is not baseline-free. This is particularly evident for scenarios in which the damage is small. Indeed, the relative difference between the quality index for damage scenario one is 34%.

Fig. 18 shows the comparison of the ACDF for the first damage scenario between the use of finite differences and cubic spline interpolation. In fact, it is clear from the analysis of this figure that the noise contamination is significantly greater if one uses finite differences. For this reason, the damage detection threshold line is considerably higher, leading to a poorer damage identification. Table 4 shows the damage localisation quality index of single damage scenarios for both approaches. It is evident that the use of cubic spline interpolation consistently achieves a better localisation quality, which is more significant for small damage. Furthermore, the vulnerability of a finite difference based approach to edge effects is also illustrated in the corresponding plot, wrongfully flagging damage at both extremities.

Recalling the results of Figs. 12, 15 and 18 and Table 4, it is clear that the scheme presented in this paper constitutes a significant improvement over other vibration-based methods previously presented.

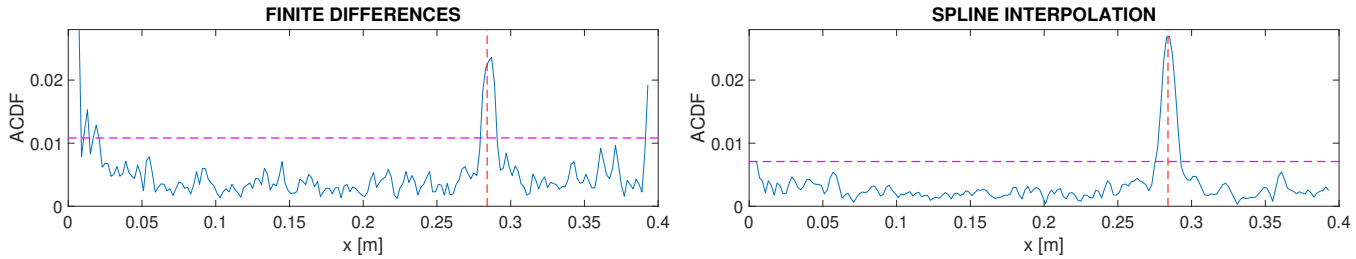

FIGURE 18 Comparison of ACDF(x) using four modes for the first damage scenario with finite differences and cubic spline interpolation.

5 | CONCLUSIONS

The technique put forward in this paper consists of a new approach for damage localisation and relative quantification based on the analysis of the modal curvature shape. The modal curvature is determined by using cubic spline interpolation as a means of differentiating the modal rotation fields, obtained experimentally with speckle shearography. Using the curvature profiles for all the available modes, the computation of two damage factors is carried out as a mean of locating and relatively quantifying damage. By analysing the results of the proposed approach, several conclusions were reached. First, the optimal spatial sampling interval was found to play a role of great importance when it comes to balancing the noise and measurement uncertainty errors and the contrast of the damage signature. Second, using the smoothing properties of the analytical derivative of the cubic spline function applied to the modal rotation field data, one is able to obtain very smooth curvature profiles with a distinct damage signature. Third, both the damage factors presented, one of which is baseline-free, successfully localises small and multiple damage, using experimental data, yielding very good results, a hurdle that a large majority of the available methods fail to overcome. Fourth, it is important to remark that the amplitude of the damage signature increases with the severity of the damage it refers to. Fifth, a comparison between finite differences and spline interpolation results, using a damage localisation quality index, shows that the best damage localisations are obtained using the latter. Sixth, throughout the analysis of the results it was possible to conclude that the present technique is very robust, consistent not only on localising the damage but also yielding a damage signature whose amplitude is identical for the same slot, when comparing single, multiple damage scenarios and computations with distinct damage factors. Finally, the novel approach to damage identification presented in this paper has a lot of potential and flexibility to be extended to plates and tridimensional structures. This analysis falls, however, out of the scope of this paper, which focus on the derivation of the optimal sampling interval and its proof of concept.

ACKNOWLEDGMENTS

This work was supported by FCT, through IDMEC, under LAETA, project UIDB/50022/2020.

Author contributions

L. Pedroso: Conceptualisation, Methodology, Software, Validation, Data curation, Writing- Original draft preparation, Writing- Reviewing and Editing, Visualisation; A. Arco: Conceptualisation, Methodology, Software, Data curation, Writing- Original draft preparation, Writing- Reviewing and Editing, Visualisation; I. Figueiras: Conceptualisation, Methodology, Software, Data curation, Writing- Original draft preparation, Writing- Reviewing and Editing, Visualisation; J.V. Araújo dos Santos: Conceptualisation, Methodology, Validation, Writing- Reviewing and Editing, Supervision, Funding acquisition; J.L.M. Fernandes: Methodology, Writing- Reviewing and Editing; H. Lopes: Conceptualization, Methodology, Validation, Investigation, Writing- Reviewing and Editing.

Conflict of interest

The authors do not have any conflicts of interest to declare.

References

1. Rytter A. Vibrational based inspection of civil engineering structures. *PhD thesis, Dept. of Building Technology and Structural Engineering, Aalborg University, Aalborg. Fracture and Dynamics* 1993.

2. Pandey AK, Biswas M, Samman MM. Damage detection from changes in curvature mode shapes. *Journal of Sound and Vibration* 1991; 145: 321-332. doi: 10.1016/0022-460X(91)90595-B

3. Zhou Z, Wegner LD, Sparling BF. Vibration-based detection of small-scale damage on a bridge deck. *Journal of Structural Engineering* 2007; 133(9): 1257–1267. doi: 10.1061/(ASCE)0733-9445(2007)133:9(1257)

4. Dilena M, Morassi A. Dynamic testing of a damaged bridge. *Mechanical Systems and Signal Processing* 2011; 25(5): 1485–1507. doi: 10.1016/j.ymssp.2010.12.017

5. Arco A, Figueiras I, Pedroso L, Araújo dos Santos, J. V. , Lopes H. Application of spline interpolation to speckle shearography measurements for damage identification. *Procedia Structural Integrity* 2019; 17: 718–725. doi: 10.1016/j.prostr.2019.08.096

6. Sazonov E, Klinkhachorn P. Optimal spatial sampling interval for damage detection by curvature or strain energy mode shapes. *Journal of Sound and Vibration* 2005; 285(4-5): 783–801. doi: 10.1016/j.jsv.2004.08.021

7. Moreno-García P, Araújo dos Santos, J. V. , Lopes H. A new technique to optimize the use of mode shape derivatives to localize damage in laminated composite plates. *Composite Structures* 2014; 108: 548–554. doi: 10.1016/j.compstruct.2013.09.050

8. Mininni M, Gabriele S, Lopes H, Araújo dos Santos, J. V. . Damage identification in beams using speckle shearography and an optimal spatial sampling. *Mechanical Systems and Signal Processing* 2016; 79: 47–64. doi: 10.1016/j.ymssp.2016.02.039

9. Francis D, Tatam RP, Groves RM. Shearography technology and applications: a review. *Measurement Science and Technology* 2010; 21(10): 102001. doi: 10.1088/0957-0233/21/10/102001

10. Araújo dos Santos, J. V. , Lopes H. Damage Localization Based on Modal Response Measured with Shearography. In: Nobari AS, Aliabadi FMH. , eds. *Vibration-Based Techniques for Damage Detection and Localization in Engineering Structures*London: World Scientific Publishing Europe. 2018 (pp. 141–172)

11. Abdel Wahab M, De Roeck G. Damage detection in bridges using modal curvatures: application to a real damage scenario. *Journal of Sound and Vibration* 1999; 226(2): 217–235. doi: 10.1006/jsvi.1999.2295

12. Chandrashekhar M, Ganguli R. Damage assessment of structures with uncertainty by using mode-shape curvatures and fuzzy logic. *Journal of Sound and Vibration* 2009; 326(3-5): 939–957. doi: 10.1016/j.jsv.2009.05.030

13. Rucevskis S, Wesolowski M. Identification of damage in a beam structure by using mode shape curvature squares. *Shock and Vibration* 2010; 17: 601–610. doi: 10.3233/SAV-2010-0551

14. Tomaszewska A. Influence of statistical errors on damage detection based on structural flexibility and mode shape curvature. *Computers & Structures* 2010; 88(3-4): 154–164. doi: 10.1016/j.compstruc.2009.08.017

15. Cao M, Radzieński M, Xu W, Ostachowicz W. Identification of multiple damage in beams based on robust curvature mode shapes. *Mechanical Systems and Signal Processing* 2014; 46(2): 468–480. doi: 10.1016/j.ymssp.2014.01.004

16. Moreno-García P, Lopes H, Araújo dos Santos, J. V. . Application of higher order finite differences to damage localization in laminated composite plates. *Composite Structures* 2016. doi: 10.1016/j.compstruct.2015.08.011

17. Chen DM, Xu YF, Zhu WD. Experimental investigation of notch-type damage identification with a curvature-based method by using a continuously scanning laser doppler vibrometer system. *Journal of Nondestructive Evaluation* 2017; 36(2): 38. doi: 10.1007/s10921-017-0418-4

18. Dahak M, Touat N, Kharoubi M. Damage detection in beam through change in measured frequency and undamaged curvature mode shape. *Inverse Problems in Science and Engineering* 2019; 27(1): 89–114. doi: 10.1080/17415977.2018.1442834

19. Feng D, Feng MQ. Output-only damage detection using vehicle-induced displacement response and mode shape curvature index. *Structural Control and Health Monitoring* 2016; 23(8): 1088–1107. doi: 10.1002/stc.1829

20. Dincal S, Stubbs N. Nondestructive damage detection in Euler-Bernoulli beams using nodal curvatures – Part I: Theory and numerical verification. *Structural Control and Health Monitoring* 2014; 21(3): 303–316. doi: 10.1002/stc.1562

21. Dincal S, Stubbs N. Nondestructive damage detection in Euler-Bernoulli beams using nodal curvatures – Part II: Field measurements. *Structural Control and Health Monitoring* 2014; 21(3): 331–341. doi: 10.1002/stc.1564

22. Rucka M, Wilde K. Application of continuous wavelet transform in vibration based damage detection method for beams and plates. *Journal of Sound and Vibration* 2006; 297(3-5): 536–550. doi: 10.1016/j.jsv.2006.04.015

23. Fan W, Qiao P. A 2-D continuous wavelet transform of mode shape data for damage detection of plate structures. *International Journal of Solids and Structures* 2009; 46(25-26): 4379–4395. doi: 10.1016/j.ijsolstr.2009.08.022

24. Rucka M. Damage detection in beams using wavelet transform on higher vibration modes. *Journal of Theoretical and Applied Mechanics* 2011; 49(2): 399–417.

25. Katunin A. Damage identification in composite plates using two-dimensional B-spline wavelets. *Mechanical Systems and Signal Processing* 2011; 25(8): 3153–3167. doi: 10.1016/j.ymssp.2011.05.015

26. Cao M, Cheng L, Su Z, Xu H. A multi-scale pseudo-force model in wavelet domain for identification of damage in structural components. *Mechanical Systems and Signal Processing* 2012; 28: 638–659. doi: 10.1016/j.ymssp.2011.11.011

27. Solís M, Ma Q, Galvín P. Damage detection in beams from modal and wavelet analysis using a stationary roving mass and noise estimation. *Strain* 2018; 54(2): e12266. doi: 10.1111/str.12266

28. Montanari L, Spagnoli A, Basu B, Broderick B. On the effect of spatial sampling in damage detection of cracked beams by continuous wavelet transform. *Journal of Sound and Vibration* 2015; 345: 233–249. doi: 10.1016/j.jsv.2015.01.048

29. Katunin A, Lopes H, Araújo dos Santos, J. V. . Identification of multiple damage using modal rotation obtained with shearography and undecimated wavelet transform. *Mechanical Systems and Signal Processing* 2019; 116: 725–740. doi: 10.1016/j.ymssp.2018.07.024

30. Zhong S, Oyadiji SO. Sampling interval sensitivity analysis for crack detection by stationary wavelet transform. *Structural Control and Health Monitoring* 2013; 20(1): 45–69. doi: 10.1002/stc.469

31. Lopes H, Ribeiro J, Araújo dos Santos, J. V. . Interferometric techniques in structural damage identification. *Shock and Vibration* 2012; 19(5): 835–844. doi: 10.3233/SAV-2012-0692

32. Golub GH, Van Loan CF. *Matrix Computations (4th Ed.)*. Baltimore: Johns Hopkins University Press. 4 ed. 2013.

33. Hoffman JD, Frankel S. *Numerical Methods for Engineers and Scientists, Second Edition,*. New York: Taylor & Francis. 2, revised ed. 2001.

34. Yueh WC. Eigenvalues of several tridiagonal matrices. *Applied Mathematics E - Notes* 2005; 5: 66–74.

35. Boor dC. *A Practical Guide to Splines*. New York: Springer-Verlag. 1 ed. 1978.

36. Conte SD, Boor dC. *Elementary Numerical Analysis: An Algorithmic Approach*. New York: McGraw-Hill. 3 ed. 1980.

37. Bauer F, Grüne L, Semmler W. Adaptive spline interpolation for Hamilton–Jacobi–Bellman equations. *Applied Numerical Mathematics* 2006; 56(9): 1196–1210. doi: 10.1016/j.apnum.2006.03.011

38. Hall CA, Meyer W. Optimal error bounds for cubic spline interpolation. *Journal of Approximation Theory* 1976; 16(2): 105–122. doi: 10.1016/0021-9045(76)90040-X

39. Zastavnik F, Pyl L, Gu J, Sol H, Kersemans M, Van Paepegem W. Comparison of Shearography to Scanning Laser Vibrometry as Methods for Local Stiffness Identification of Beams. *Strain* 2014; 50(1): 82–94. doi: 10.1111/str.12069

40. Lopes H, Araújo dos Santos, J. V. , Moreno-García P. Evaluation of noise in measurements with speckle shearography. *Mechanical Systems and Signal Processing* 2019; 118: 259–276. doi: 10.1016/j.ymssp.2018.08.042

41. Cao MS, Xu W, Ren WX, Ostachowicz W, Sha GG, Pan LX. A concept of complex-wavelet modal curvature for detecting multiple cracks in beams under noisy conditions. *Mechanical Systems and Signal Processing* 2016; 76-77: 555–575. doi: 10.1016/j.ymssp.2016.01.012